Hyperbolic geometry of structure matrices in a hierarchical texture-descriptor tensor: multiscale texture of grapevine leaves and wood affected by esca

Ştefan Ţălu

The Directorate of Research, Development and Innovation Management (DMCDI), The Technical University of Cluj-Napoca, Cluj-Napoca, Romania. Corresponding author: Ş. Ţălu, stefan.talu@auto.utcluj.ro

https://doi.org/10.67784/0100

Abstract. Esca of grapevine produces foliar symptoms and internal wood necrosis that are scored visually, by severity class. This study extends a hierarchical texture-descriptor tensor, indexed by descriptor channel, Gaussian scale, orientation and region of interest, with four results needed for plant tissue, and applies it to published colour photographs of *Vitis vinifera* 'Malvasia Fina' leaves and trunk cross-sections at four severity levels (control, asymptomatic, chlorotic, scorched), and to an external esca-affected trunk section with zones labelled by its authors. The theory shows (i) that the affine-invariant distance between two structure matrices splits exactly into an energy term and a hyperbolic term in which the pair (anisotropy A, doubled texture axis 2ψ) are Beltrami–Klein disk coordinates, so that changes of contrast, of anisotropy and of orientation are separated, and only the first changes under a global photographic gain; (ii) that the orientation profile of the mean absolute directional derivative contains the second and fourth circular moments of gradient orientation with weights 1/3 and 1/15, the fourth being recoverable only with eight orientations; (iii) that pooling over colour channels obeys the same inequality as pooling over regions; and (iv) that a moving radial–tangential frame removes the cancellation of radial anatomy in pooled estimates. On leaves, the global anisotropy index depended on where the analysed region lay relative to the main veins, whereas the mean local coherence fell from 0.30–0.34 in symptomless leaves to 0.19 in symptomatic leaves (Kendall $\tau = -0.38$ across 141 blocks of the four leaves, a within-image descriptive test, $P < 10^{-8}$), and the decrease persisted after a common blur; the asymptomatic leaf of an infected vine was not distinguished from the control ($P = 0.60$). In trunk sections, ray-dominated texture (radiality index $\rho > 0$) in the outer wood gave way to concentric texture with increasing severity (outer mean ρ from +0.13 to −0.21). In the external section, white rot, the interaction border and sectorial necrosis were separated from healthy wood mainly by rotation, anisotropy and energy, respectively, and the texture axis turned by about 90° about 110 px inside the colour edge. The results provide interpretable, contrast-aware texture readings on the analysed agronomic images; they are exploratory, and diagnostic value is not claimed.
Keywords: grapevine trunk diseases, esca, *Vitis vinifera*, texture analysis, structure tensor, descriptor tensor, hyperbolic geometry, anisotropy, plant phenotyping.

Introduction. Grapevine trunk diseases are among the most destructive diseases of *Vitis vinifera* worldwide, and esca is the most widespread of them (Mugnai et al., 1999; Bertsch et al., 2013; Kenfaoui et al., 2022). Its expression is twofold. In the trunk, cross-sections show black spots and streaks in the xylem, brown to dark necrosis around the pith and, in older vines, a soft white rot separated from sound wood by a dark border (Mugnai et al., 1999; Kenfaoui et al., 2022). In the canopy, leaves develop interveinal chlorosis that progresses to the characteristic "tiger-stripe" necrosis, often erratically from year to year, and vines may carry wood symptoms while their leaves remain symptomless (Lecomte et al., 2012; Claverie et al., 2020). Field assessment therefore relies on visual severity classes, and the relation between leaf and wood symptoms remains the object of active research (Lecomte et al., 2012; Goufo et al., 2022).

Image-based measurement is the natural complement of visual scoring. Plant disease detection by digital images and imaging sensors has been reviewed extensively (Barbedo, 2013; Mahlein, 2016), and most methods segment lesions by colour and report their area or count. Texture analysis offers a different route: it describes how intensity varies in space, through statistics of differences, co-occurrences, filter

responses or scaling behaviour, without requiring lesions to be segmented (Haralick et al., 1973; Ţălu, 2012; Depeursinge, 2017; Ghalati et al., 2022). Leaf and wood symptoms of esca are well suited to it: chlorosis and necrosis interrupt the oriented pattern of the venation, and wood necrosis replaces the radial pattern of rays and vessels with concentric or irregular discolouration. Fractal, multifractal and lacunarity descriptors, which quantify scale-dependent complexity, have been applied to biological and tissue surfaces and images (Ţălu & Giovanzana, 2011; Ţălu, 2013, 2015; Ţălu et al., 2015; Garczyk et al., 2017) and to aquaculture (Petrescu-Mag et al., 2026); orientation-resolved descriptors have received less attention in plant pathology.

Two difficulties limit the transfer of texture descriptors from histology to agronomic photographs. First, texture depends jointly on the scale at which it is observed, the direction in which it is probed and the region over which it is summarized (Depeursinge, 2017), and in plant organs the dominant direction varies systematically across the organ: veins radiate from the petiolar junction, and rays radiate from the pith. A single orientation summary over a region then cancels structure that is locally strong. Second, field photographs differ in exposure, white balance and resolution, so a change in a descriptor may reflect the camera rather than the tissue (Traverso et al., 2018; Zwanenburg et al., 2020). Any comparison between photographs needs to state which part of a descriptor change can be produced by photographic gain.

A hierarchical descriptor tensor that keeps scale, orientation and region as separate indices of every measurement was introduced for muscle histology (Ţălu, 2027a), applied to guppy, porcine and rabbit muscle (Ţălu, 2026, 2027b, 2027c) and extended to soil thin sections (Ţălu, 2027d). The present study extends it to plant tissue. Its contributions are theoretical and applied. On the theoretical side, it derives an exact decomposition of the distance between two structure matrices into a contrast-dependent energy term and contrast-invariant anisotropy and rotation terms, through the Beltrami–Klein model of the hyperbolic plane; the harmonic content of the orientation profile of the mean absolute derivative; the colour form of the pooling inequality; and a moving radial–tangential frame for organs with radial anatomy. On the applied side, it analyses published photographs of grapevine leaves and trunk cross-sections at four esca severity levels (Goufo et al., 2022) and, as an external check, a published trunk section in which the zones of white rot, interaction border, sectorial necrosis and healthy wood were labelled by its authors (Kenfaoui et al., 2022). Because the images are single published examples without replicates, the aim is to establish whether the tensor gives interpretable and internally consistent readings on agronomic images, and which of them are robust to differences between photographs, not to evaluate diagnostic performance.

Theoretical Framework

Hierarchical descriptor tensor. Let $f(\mathbf{x})$, $\mathbf{x} \in \Omega \subset \mathbb{R}^2$, be an image channel, and $G_s = g_s * f$ its Gaussian scale-space at scale s (Lindeberg, 1998). With the unit vector $\mathbf{u}_\theta = (\cos\theta, \sin\theta)^\mathsf{T}$ (angle counter-clockwise from the image rows, y axis upward), the steerable directional derivative is $\partial_\theta G_s = \mathbf{u}_\theta \cdot \nabla G_s$ (Freeman & Adelson, 1991). For regions $\Omega_1, \ldots, \Omega_R$, each channel m summarizes a local response over a region, and the measurements form the array

$$\mathfrak{D}_{mklr} = D_m(s_k, \theta_l, \Omega_r), \qquad \mathfrak{D} \in \mathbb{R}^{M\times K\times L\times R} \qquad (1)$$

with $M = 10$ channels (directional-derivative statistics D1–D5, grey-level co-occurrence features D6–D9 and autocorrelation D10), $K = 4$ scales ($s = 1, 2, 4, 8$ px), $L = 4$ orientations ($\theta = 0, \pi/4, \pi/2, 3\pi/4$) and $R = 1$ or 4 regions, as defined in the original formulation (Ţălu, 2027a). Two channels are central here: the mean absolute derivative D1 $= \langle|\partial_\theta G_s|\rangle_r$ and the directional energy D2 $= \langle(\partial_\theta G_s)^2\rangle_r$. With the regional structure matrix (Bigün & Granlund, 1987)

$$\mathbf{J}_{s,r} = \langle \nabla G_s \, \nabla G_s^\mathsf{T} \rangle_r, \qquad D_2(\theta) = \mathbf{u}_\theta^\mathsf{T} \mathbf{J}_{s,r} \mathbf{u}_\theta = 1/2\,(\lambda_+ + \lambda_-) + 1/2\,(\lambda_+ - \lambda_-)\cos 2(\theta - \varphi) \qquad (2)$$

where $\lambda_+ \geq \lambda_-$ are the eigenvalues of $\mathbf{J}$ and φ the direction of its leading eigenvector (Proposition 1 of Ţălu, 2027a). The anisotropy index and the texture axis are

$$A = \frac{\lambda_+ - \lambda_-}{\lambda_+ + \lambda_-}, \qquad \psi = \varphi + \frac{\pi}{2} \ (\mathrm{mod}\ \pi) \qquad (3)$$

and are determined exactly by the four D2 entries. Writing β for the gradient direction and $z = |\nabla G_s|^2\, e^{2i\beta}$, $A = |\langle z\rangle_r|/\langle|z|\rangle_r$ is the energy-weighted mean resultant length of the doubled gradient direction (Mardia & Jupp, 2000), and for a partition into equal-area regions with energies $E_r = \mathrm{tr}\,\mathbf{J}_{s,r}$ the pooling inequality holds (Proposition 2 of the same study):

$$A(\Omega) \le \frac{\sum_r E_r\, A_r}{\sum_r E_r} \qquad (4)$$

with equality if and only if all regions share the same texture axis. Replacing the regional mean by a Gaussian window of width ω gives the structure-tensor field $\mathbf{J}_{s,\omega}(\mathbf{x})$ and its local coherence $\kappa(\mathbf{x}) = (\lambda_+ - \lambda_-)/(\lambda_+ + \lambda_-)$ (Kass & Witkin, 1987; Bigün & Granlund, 1987). Because the windowed field is a convex combination of local doubled-angle vectors, the argument of (4) gives $A(\Omega) \le \overline{\kappa}_E$, the energy-weighted mean of κ over Ω; the ratio $A(\Omega)/\overline{\kappa}_E \in [0, 1]$ is used below as the *pooling ratio*: it is 1 when local orientations agree across the region and small when strong local orientation is cancelled by its variation across the region, as in a leaf crossed by radiating veins.

Angular harmonics of the mean absolute derivative. The directional energy D2 is a quadratic form in $\mathbf{u}_\theta$ and therefore contains only the angular harmonics of orders 0 and 2. D1 is not quadratic, and its orientation profile carries more information. Let $c_n = L^{-1}\,\Sigma_l\, \mathrm{D1}(\theta_l)\, e^{-in\theta l}$ denote its discrete Fourier coefficients, and define the normalized harmonics $R_2 = |c_2|/c_0$ and $R_4 = |c_4|/c_0$.

Proposition 3 (harmonic content of D1). For continuous orientation,

$$D_1(\theta) = \frac{2}{\pi}\langle|\nabla G_s|\rangle_r\left[1 + 2/3\ \mathrm{Re}\left(\bar{m}_2\, e^{2i\theta}\right) - 2/15\ \mathrm{Re}\left(\bar{m}_4\, e^{4i\theta}\right) + \cdots\right], \qquad m_n = \frac{\langle|\nabla G_s|\, e^{in\beta}\rangle_r}{\langle|\nabla G_s|\rangle_r} \qquad (5)$$

so that $R_2 = |m_2|/3$ and $R_4 = |m_4|/15$, where m_2 and m_4 are the magnitude-weighted second and fourth circular moments of the gradient direction. These are identities for the continuous orientation profile; the sampled coefficients c_n differ from them only by the aliased orders, for which bounds are given below. For the energy channel, the coefficient of order 4 vanishes identically. With $L = 4$ equally spaced orientations, only the alternating component $a_4 = (\mathrm{D1}(0) - \mathrm{D1}(\pi/4) + \mathrm{D1}(\pi/2) - \mathrm{D1}(3\pi/4))/(4c_0)$ is available, and $a_4 = -(2/15)\ \mathrm{Re}\ m_4$ plus aliased harmonics of orders 12, 20, …; it depends on the rotation of the image. With $L = 8$, $|c_4|$ is available and R_4 is rotation invariant up to aliasing.

Proof. Pointwise, $|\partial_\theta G_s| = |\nabla G_s|\ |\cos(\theta - \beta)|$, and $|\cos x| = 2/\pi + (4/3\pi)\cos 2x - (4/15\pi)\cos 4x + \Sigma_{n\ge3}\ (-1)^{n+1}\, 4/(\pi(4n^2 - 1))\cos 2nx$. Averaging over Ω_r is linear and gives (5). $(\partial_\theta G_s)^2 = |\nabla G_s|^2(1 + \cos 2(\theta - \beta))/2$ has no harmonic of order 4. At $\theta_l = l\pi/4$, $e^{4i\theta l} = (-1)^l$ is real, so the order-4 term equals $-(2/15)(-1)^l\ \mathrm{Re}\ m_4$ and $\mathrm{Im}\ m_4$ is not sampled; the harmonics of orders $4 + 8j$ fold onto the same alternating sequence. With $L = 8$, $e^{4i\theta l} = i^l$ separates $\mathrm{Re}\ m_4$ and $\mathrm{Im}\ m_4$, and only orders 12, 20, … fold onto order 4.

The aliasing is bounded and small. For a single gradient direction, the worst case, $|a_4 + (2/15)\cos 4\beta| \le 0.038$ with $L = 4$, and $-0.008 \le R_4 - 1/15 \le 0.016$ and $-0.009 \le R_2 - 1/3 \le 0.018$ with $L = 8$ (computed numerically over all β; for a texture with several directions the deviations are averages of these and therefore smaller in magnitude). Two consequences matter for plant tissue. First, R_4 distinguishes structure that A cannot: two families of lines at right angles with equal weight give $A = 0$ and $m_2 = 0$, but $|m_4| = 1$ if they occupy disjoint supports, whereas families at 45° cancel m_4 and not m_2. A network of crossing veins is therefore expected to show $R_4 > 0$ where A is small. Second, the identity $c_4(\mathrm{D2}) = 0$ is a computational check that holds for every $L \ge 8$, complementing the four-orientation check $\mathrm{D2}(0) + \mathrm{D2}(\pi/2) = \mathrm{D2}(\pi/4) + \mathrm{D2}(3\pi/4)$.

Colour structure tensor. Plant symptoms are chromatic: chlorosis is a loss of green and necrosis a shift to brown. For a multichannel image the gradient structure is described by the sum of the channel structure matrices (Di Zenzo, 1986). Working in CIELAB (CIE, 2004), where Euclidean differences approximate perceived colour differences, let $\mathbf{J}_\mathrm{L}$, $\mathbf{J}_\mathrm{a}$, $\mathbf{J}_\mathrm{b}$ be the structure matrices of L^*, a^* and b^*, and $\mathbf{J}_\mathrm{Lab} = \mathbf{J}_\mathrm{L} + \mathbf{J}_\mathrm{a} + \mathbf{J}_\mathrm{b}$.

Corollary 1 (colour pooling). With $E_c = \mathrm{tr}\,\mathbf{J}_c$ and A_c the anisotropy of channel c,

$$A(\mathbf{J}_{Lab}) \le \frac{\sum_c E_c\, A_c}{\sum_c E_c}, \qquad \chi = \frac{\mathrm{tr}(\mathbf{J}_a + \mathbf{J}_b)}{\mathrm{tr}\,\mathbf{J}_{Lab}} \in [0,1] \qquad (6)$$

with equality in the first relation if and only if all channels share the same texture axis. *Proof*. The doubled-angle vector of $\mathbf{J}_{\mathrm{Lab}}$ is the sum of those of the channels, and the triangle inequality applies as in (4). The *chromatic energy fraction* χ is the share of gradient energy carried by colour rather than by lightness; it is defined only in a perceptual space in which the channels share units, which is why CIELAB rather than RGB is used.

Geometry of structure matrices. Comparing two regions, two images or two zones of a lesion requires a distance between structure matrices. Structure matrices are symmetric positive definite (SPD), and the natural distance on SPD matrices is the affine-invariant Riemannian distance $d(\mathbf{J}_1, \mathbf{J}_2) = \|\log(\mathbf{J}_1^{-1/2}\mathbf{J}_2\mathbf{J}_1^{-1/2})\|_F$ (Moakher, 2005; Pennec et al., 2006; Bhatia, 2007). For 2 × 2 matrices it has an exact and interpretable decomposition.

Proposition 4 (Klein-disk decomposition). Let $\mathbf{J}_1$, $\mathbf{J}_2$ be 2 × 2 SPD matrices with anisotropy indices A_1, A_2 and texture axes ψ_1, ψ_2, and $\Delta\psi = \psi_2 - \psi_1$. Then

$$d^2(\mathbf{J}_1, \mathbf{J}_2) = 1/2 \ln^2 \frac{\det \mathbf{J}_2}{\det \mathbf{J}_1} + 2\, d_K^2, \qquad \cosh d_K = \frac{1 - A_1 A_2 \cos 2\Delta\psi}{\sqrt{(1 - A_1^2)(1 - A_2^2)}} \qquad (7)$$

where d_K is the distance between the points $z_i = A_i e^{2i\psi i}$ in the Beltrami–Klein model of the hyperbolic plane of curvature −1 (Ratcliffe, 2006).

Proof. Write $\mathbf{J}_i = (\det \mathbf{J}_i)^{1/2}\, \mathbf{S}_i$ with $\det \mathbf{S}_i = 1$. The eigenvalues of $\mathbf{J}_1^{-1/2}\mathbf{J}_2\mathbf{J}_1^{-1/2}$ are $(\det \mathbf{J}_2/\det \mathbf{J}_1)^{1/2}\, e^{\pm\delta/2}$, where $e^{\pm\delta/2}$ are those of $\mathbf{S}_1^{-1/2}\mathbf{S}_2\mathbf{S}_1^{-1/2}$; hence $d^2 = \tfrac{1}{2} \ln^2(\det \mathbf{J}_2/\det \mathbf{J}_1) + \delta^2/2$. With $\ell_i = \operatorname{artanh} A_i$, (3) gives $\lambda_+/\lambda_- = e^{2\ell_i}$, so $\mathbf{S}_i = \mathbf{R}(\varphi_i)\, \mathrm{diag}(e^{\ell_i}, e^{-\ell_i})\, \mathbf{R}(\varphi_i)^{\mathsf{T}}$. A direct computation gives $2\cosh(\delta/2) = \mathrm{tr}(\mathbf{S}_1^{-1}\mathbf{S}_2) = 2[\cosh \ell_1 \cosh \ell_2 - \sinh \ell_1 \sinh \ell_2 \cos 2\Delta\psi]$. Factoring out $\cosh \ell_1 \cosh \ell_2 = [(1 - A_1^2)(1 - A_2^2)]^{-1/2}$ gives the second relation in (7) with $d_K = \delta/2$, which is the Beltrami–Klein distance between points of Euclidean radius $A_i = \tanh \ell_i$ and polar angle $2\psi_i$.

Three consequences are used throughout (Figure 1). First, the pair $(A, 2\psi)$ is not an ad hoc polar plot: it is the natural coordinate system of the shape of a structure matrix, with isotropic textures at the centre and perfectly oriented textures on the boundary, and the anisotropy index is the Euclidean radius of the point in the Klein disk (its hyperbolic radius is artanh A). Second, d_K splits into an aligned part and a rotation excess, so that

$$d^2 = \underbrace{1/2 \ln^2 \frac{\det \mathbf{J}_2}{\det \mathbf{J}_1}}_{\text{energy}} + \underbrace{2(\operatorname{artanh} A_1 - \operatorname{artanh} A_2)^2}_{\text{anisotropy}} + \underbrace{2[d_K^2 - (\operatorname{artanh} A_1 - \operatorname{artanh} A_2)^2]}_{\text{rotation}} \qquad (8)$$

with all three terms non-negative and the last zero if and only if $\Delta\psi = 0$ or one of the textures is isotropic. Third, a global gain $f \to cf$ multiplies $\mathbf{J}$ by c^2 and changes only the energy term, which equals $8 \ln^2 c$, i.e. $d = 2\sqrt{2}\, |\ln c|$, when $\mathbf{J}_2 = c^2\mathbf{J}_1$; the anisotropy and rotation terms are invariant to photographic contrast. When images are taken under different illumination, only the last two terms can be compared between images without calibration. In the analyses below each photograph is standardized separately, which cancels a pure global gain; the energy term nevertheless remains sensitive to acquisition factors that standardization does not remove (focus, non-linear exposure, non-uniform illumination, background and crop composition). In tables and figures the three terms are reported as their square roots, which have the units of d and satisfy $d^2 = (\sqrt{\text{energy}})^2 + (\sqrt{\text{anisotropy}})^2 + (\sqrt{\text{rotation}})^2$.

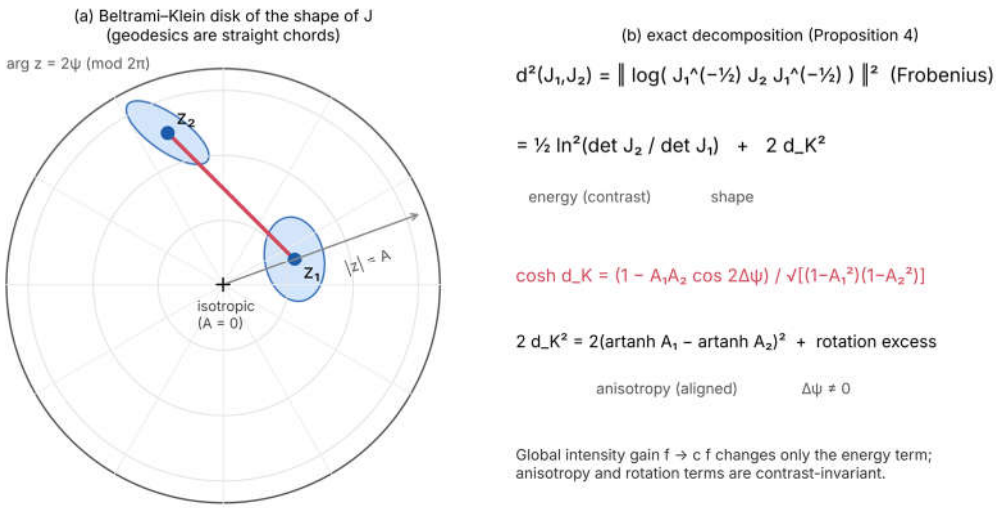


Figure 1. Geometry of structure matrices. (a) The shape of a 2 × 2 structure matrix **J** (glyph: ellipse with axes proportional to $\sqrt{\lambda_\pm}$) is a point $z = Ae^{2i\psi}$ of the Beltrami–Klein disk; isotropic textures lie at the centre and perfectly oriented textures on the boundary; geodesics of the model are straight chords (red). (b) Exact decomposition of the affine-invariant distance (Proposition 4): an energy term that depends on photographic contrast, and an anisotropy term and a rotation term that do not.

Moving frame for radial anatomy. In a transverse section of a stem or trunk, rays and vessels radiate from the pith, and growth rings and necrotic fronts are concentric. Pooled over the whole section in image coordinates, radial structure has no preferred direction, and by (4) its anisotropy is close to zero regardless of how strongly radial it is. The cancellation is removed by expressing gradients in the radial–tangential frame of a centre **c**: with $\phi(\mathbf{x})$ the polar angle of $\mathbf{x} - \mathbf{c}$, let $g_r = \nabla G_s \cdot \mathbf{e}_r$ and $g_t = \nabla G_s \cdot \mathbf{e}_t$, and

$$\mathbf{J}_{s,r}^{rt} = \begin{pmatrix} \langle g_r^2 \rangle_r & \langle g_r g_t \rangle_r \\ \langle g_r g_t \rangle_r & \langle g_t^2 \rangle_r \end{pmatrix}, \qquad \rho = \frac{\langle g_t^2 \rangle_r - \langle g_r^2 \rangle_r}{\langle g_t^2 \rangle_r + \langle g_r^2 \rangle_r} \in [-1,1] \qquad (9)$$

Proposition 5 (radiality). $\mathbf{J}^{rt}$ is invariant to rotations of the image about **c**; $\rho = +1$ for texture made of straight lines through **c** (rays), $\rho = -1$ for circles centred on **c** (rings), $\rho = 0$ for an isotropic texture, and $|\rho| \le A(\mathbf{J}^{rt})$. The pooling inequality (4) holds for $\mathbf{J}^{rt}$ over any union of regions.

Proof. Rotation by a about **c** rotates both ∇G_s and the frame ($\mathbf{e}_r$, $\mathbf{e}_t$) by a, leaving g_r, g_t unchanged. Along a ray, gradients are perpendicular to the ray, i.e. tangential ($g_r = 0$); across a ring they are radial ($g_t = 0$). For isotropic texture $\langle g_r^2 \rangle = \langle g_t^2 \rangle$. $\rho = (J_{tt} - J_{rr})/\mathrm{tr}\,\mathbf{J}^{rt}$ is the projection of the doubled-angle vector of $\mathbf{J}^{rt}$ on its first axis, whose length is A. (4) holds for any family of 2 × 2 positive semidefinite matrices. ■

Positive ρ thus indicates ray-dominated texture and negative ρ concentric texture, in a form that, unlike a polar resampling of the image, involves no interpolation and no change of pixel geometry with radius.

Reference for isotropy and uncertainty. As in the earlier muscle studies, two constructions replace the missing replicates. Isotropic surrogates, generated from the radially averaged Fourier amplitude of each image with random phases (Theiler et al., 1992), provide the finite-sample floor of A and of the harmonics R_2, R_4 for the same region size and radial spectrum; and a block bootstrap (Künsch, 1989) provides percentile intervals of A and ψ. Surrogates test departure from an isotropic spectrum; they are Gaussian and do not reproduce the non-Gaussian intensity distribution of plant tissue.

Materials and Methods

Test images. The main data set is Figure 1 of Goufo et al. (2022), which shows, for *Vitis vinifera* 'Malvasia Fina' plants from a naturally infected vineyard, one leaf and one trunk

cross-section for each of four classes: healthy leaves (control) from vines with unaffected wood; healthy-looking (asymptomatic) leaves from wood-infected vines; chlorotic leaves (symptom severity level 1) and scorched leaves (symptom severity level 2) from wood-infected vines (Figure 2). The four classes are referred to as severity levels 0–3, and the leaves and sections as F0–F3 and L0–L3. The leaves show the progression from a uniform green blade with a fine reticulate venation (F0, F1) to diffuse interveinal chlorotic spots (F2) and to the confluent yellow–green "tiger-stripe" pattern with red-brown necrotic flecks (F3). The sections show the radial pattern of rays in sound wood (L0), a ring of black spots around the pith (L1), a dark necrotic ring around the pith (L2) and extensive central necrosis (L3).

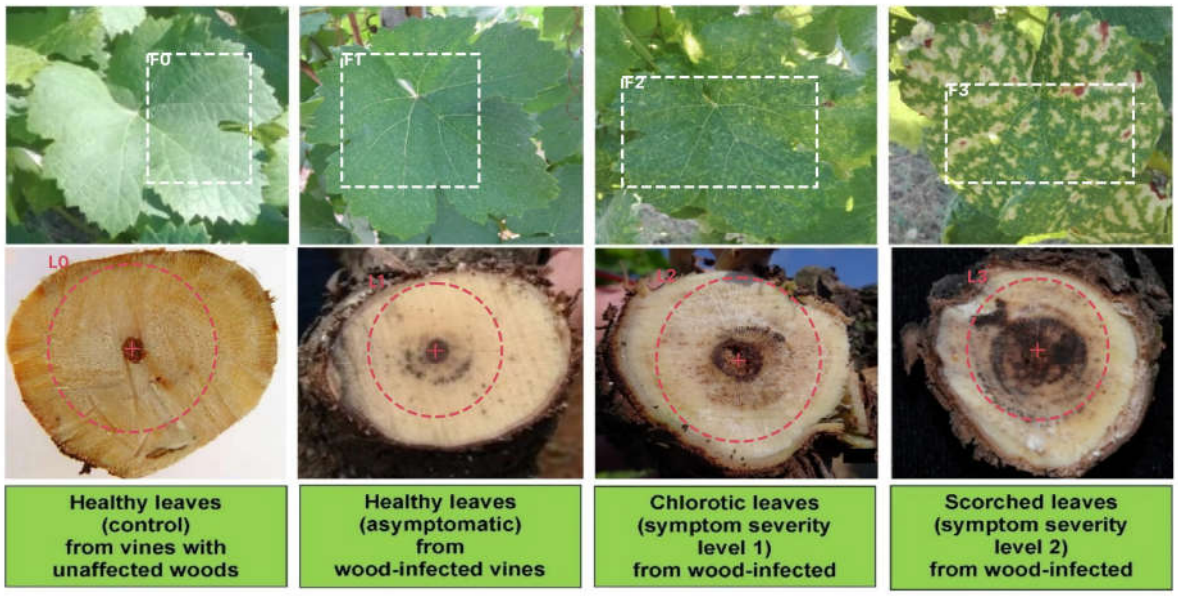


Figure 2. Source images and analysed regions. Leaves (top) and trunk cross-sections (bottom) of *Vitis vinifera* 'Malvasia Fina' at four esca severity levels; dashed white rectangles: leaf regions F0–F3; dashed red circles: outer radius *R* of the wood analysis around the pith (+). Image reproduced from Goufo et al. (2022), Figure 1, under the CC BY licence; overlays added by the author.

An external trunk section was taken from Figure 4b of Kenfaoui et al. (2022) (lower panel), in which the authors labelled healthy wood (B), white rot (A), the interaction zone or border between white rot and healthy wood (L), black spots (P) and sectorial necrosis (S). This image was used only to check whether the tensor separates zones defined by plant pathologists and locates the boundary between healthy and affected wood.

Image sources and permission to reproduce. Both source articles are open access and distributed under the Creative Commons Attribution (CC BY) licence (Goufo et al., 2022; Kenfaoui et al., 2022), which permits reuse, adaptation and redistribution in any medium provided that the original work is properly cited. The images are reproduced with overlays only; all derived panels (Figures 3–7) are new analyses produced by the author. The sources are cited in each caption.

Analysis configuration. The figure of Goufo et al. (2022) was analysed as a 3088 × 1572 px RGB raster; the panel of Kenfaoui et al. (2022) was extracted from the article PDF as embedded (1750 × 1185 px after cropping to the lower section of panel 4b). No scale bar is available, so all lengths are in pixels. Leaves were analysed in rectangular regions placed inside the leaf blade so as to exclude background, leaf margins and other leaves (Figure 2, Table 1); in F0 a tendril crossing the blade (5.3 % of the region) and in F1 a specular highlight at the petiolar junction (3.2 %) were removed by fast-marching

inpainting (Telea, 2004). ROI = 1 is the region left after a 24-px margin, which equals three standard deviations of the largest Gaussian kernel (s = 8 px); ROI = 4 is its partition into equal quadrants (1, upper left; 2, upper right; 3, lower left; 4, lower right). Derivative filters were applied to the whole crop with reflection at the borders and aggregated over each ROI. The ten-channel tensor and A, ψ were computed on the z-scored luminance Y = 0.299R + 0.587G + 0.114B, exactly as in the muscle studies; the colour quantities (Corollary 1) were computed on CIELAB coordinates in their natural units (sRGB, D65; CIE, 2004).

Local measures were computed at s = 2 px with a window ω = 16 px. To compare classes, each leaf ROI was tiled into non-overlapping blocks of 48 × 48 px (24, 36, 45 and 36 blocks for F0–F3), and in each block the local coherence $\overline{\kappa}$ (mean of $\kappa(\mathbf{x})$ over the block, L^* channel), the block anisotropy A, the chromatic energy fraction χ and the harmonic R_4 of D1 (L = 8) were computed. Trends with severity level were tested with Kendall's τ over all blocks (Kendall, 1938) and pairs of classes with the Mann–Whitney test (Mann & Whitney, 1947). Blocks within a leaf are spatially correlated, so P-values describe the separation of block distributions within these images, not a population inference. Because F0 is visibly less sharp and more brightly exposed than F1–F3, all leaf analyses were repeated after a common Gaussian blur of σ = 1.5 px applied to all four crops, which equalizes the high-frequency content that differs between photographs.

For the trunk sections, the pith was located visually and the outer radius R was chosen inside the wood, excluding bark (R = 220, 175, 215 and 185 px for L0–L3; Figure 2). The disc was divided into eight equal-width annuli between 12 px and R, and in each annulus the radial–tangential matrix $\mathbf{J}^{rt}$ (9), the radiality ρ, the mean L^* and the chromatic fraction χ were computed at s = 2 and 4 px. The radius at which L^* reaches the midpoint between its innermost and outermost values was taken as the colour front, and compared with the annulus of minimum ρ. Distances to the control were computed with (7)–(8) between whole-disc $\mathbf{J}^{rt}$ matrices, and, within each section, between each annulus and the outermost annulus.

For the external section, rectangular zones were placed beside the authors' letters B, A, L and S, avoiding the letters themselves (Figure 7a), and compared with the healthy zone B by (7)–(8) at s = 2, 4 and 8 px (local coherence with ω = 8 px because of the zone size). In addition, a vertical transect 219 px wide crossing from healthy wood (B) through the dark border band was analysed with a sliding window of 131 px height and 16 px step; at each position the texture axis ψ, L^* and the distance (8) to the first (healthy) window were recorded.

Uncertainty and isotropic floors followed the earlier muscle studies: 8 × 8 block bootstrap with 1000 resamples for ROI = 1 (6 × 6 blocks and 500 resamples for each quadrant of ROI = 4), and 200 isotropic surrogates for A (100 for R_2 and R_4), with P = (1 + n≥)/(1 + N), where n≥ is the number of the N surrogates whose value is at least the observed one, so that the smallest attainable P is 1/201 = 0.005. The bootstrap divides the ROI into a grid of 8 × 8 (or 6 × 6) blocks, not blocks of 8 px. Tests repeated over scales, regions and classes are not corrected for multiplicity and are read descriptively. The analysis geometry is summarized in Table 1.

Table 1
Test images and analysis geometry (W × H in px). Sources: Goufo et al. (2022), Figure 1 (F, L); Kenfaoui et al. (2022), Figure 4b (J)

Image	*Class (severity level)*	*Analysed region*	*ROI = 1 (after margin)*	*Notes*
F0	Healthy leaf, control vine (0)	270 × 340	222 × 292	Softer, brighter exposure; tendril inpainted (5.3 %)
F1	Asymptomatic leaf, infected vine (1)	360 × 350	312 × 302	Contains petiolar junction; highlight inpainted (3.2 %)
F2	Chlorotic leaf (2)	510 × 290	462 × 242	Contains petiolar junction
F3	Scorched leaf (3)	490 × 260	442 × 212	Red-brown necrotic flecks included
L0	Trunk section, control vine (0)	disc, R = 220	8 annuli, 12–220	White background, different lighting
L1	Trunk section, asymptomatic (1)	disc, R = 175	8 annuli, 12–175	Low effective resolution
L2	Trunk section, level 1 (2)	disc, R = 215	8 annuli, 12–215	Dark necrotic ring
L3	Trunk section, level 2 (3)	disc, R = 185	8 annuli, 12–185	Extensive central necrosis
J	Esca-affected section with labelled zones	1750 × 1185	4 zones, 1 transect	Soft raster; letters avoided

Software and verification. The analysis was implemented in Python (NumPy, SciPy, OpenCV). The ten-channel tensor reproduces the reference implementation of the original formulation. The new quantities were verified on synthetic textures (single line families at all orientations, orthogonal and 60° crossings, isotropic Gaussian noise) and Proposition 4 on 2000 pairs of random SPD matrices; the maximum relative difference between (7) and the direct matrix-logarithm distance was 3×10^{-14}.

Results

Verification of the angular harmonics. Table 2 and Figure 5a compare the harmonics of D1 with Proposition 3 on synthetic line textures. For a single line family, R_2 = 0.33–0.35 and R_4 = 0.06–0.08 at all orientations, against the predicted 1/3 and 1/15, the deviations being within the aliasing bounds; the four-orientation component a_4 instead varied between −0.172 and +0.172 with the orientation of the lines, confirming that it is not rotation invariant. Two families at right angles gave A = 0 and R_2 = 0 but R_4 = 0.023–0.026; the value is below 1/15 because the two gratings were superimposed rather than disjoint, so that gradients add vectorially where they cross. Three families at 60° and isotropic noise gave $R_4 \leq 0.003$. The order-4 coefficient of D2 was below 10^{-16} in every case.

Table 2
Verification of Proposition 3 on synthetic textures (512 × 512 px, s = 2 px, period 12 px). R_2, R_4: normalized harmonics of D1 with L = 8; a_4: alternating component with L = 4

Texture	*A*	*R_2*	*R_4*	*a_4 (L = 4)*	*$\lvert c_4(D2)\rvert/c_0$*
One family, 0°	1.000	0.351	0.082	−0.172	5×10^{-17}
One family, 30°	1.000	0.327	0.061	+0.054	4×10^{-17}
Orthogonal, 0°/90°	0.000	0.000	0.023	+0.047	0
Orthogonal, 22.5°/112.5°	0.000	0.000	0.026	0.000	4×10^{-17}
Three families, 0°/60°/120°	0.002	0.000	0.003	−0.005	8×10^{-17}
Isotropic Gaussian noise	0.009	0.002	0.000	+0.001	4×10^{-17}
Prediction, one family	1	1/3	1/15	$-(2/15)\cos 4\beta$	0

Leaves: regional anisotropy and texture axis. Table 3 gives the single-ROI anisotropy index and texture axis of the four leaves. All four exceeded their isotropic floor at s = 1–4 px (P = 0.005); at s = 8 px, F2 and F3 remained significant, while F0 (P = 0.62) and F1 (P = 0.91) did not. The ordering of A did not follow severity: the control leaf had the highest value (0.251 at s = 2 px) and the asymptomatic leaf the lowest (0.062), with the chlorotic and scorched leaves in between (0.096 and 0.090). The texture axis

was 119° in F0, 68° in F1 and close to the horizontal in F2 and F3 (173° and 180°). The four-orientation identity D2(0) + D2(π/2) = D2(π/4) + D2(3π/4) held to within 3×10^{-16}.

Table 3

Leaves, ROI = 1: anisotropy index *A* at four scales, 95 % bootstrap CI and isotropic floor (95th percentile of 200 surrogates) at *s* = 2 px, P-value at *s* = 2 and 8 px, texture axis *ψ* and characteristic scale *s** (luminance *Y*)

Leaf	*A (s = 1)*	*A (s = 2) [95 % CI]*	*A (s = 4)*	*A (s = 8)*	*Floor (s = 2)*	*P (s = 2 / 8)*	*ψ (s = 2)*	*s* (px)*
F0	0.247	0.251 [0.186, 0.334]	0.166	0.158	0.064	0.005 / 0.62	118.9°	≥ 16 (edge)
F1	0.044	0.062 [0.017, 0.177]	0.072	0.045	0.022	0.005 / 0.91	67.9°	1.31
F2	0.113	0.096 [0.047, 0.143]	0.112	0.169	0.022	0.005 / 0.005	172.7°	2.05
F3	0.075	0.090 [0.044, 0.144]	0.113	0.167	0.035	0.005 / 0.005	179.7°	6.61

Interpretation. The global *A* of a leaf region is dominated by the geometry of the venation within it, not by the symptoms. F1 contains the petiolar junction, from which the main veins radiate in all directions; their orientations cancel in the regional average, and *A* is small although the veins are sharp. F0 contains only part of one lobe, crossed by nearly parallel secondary veins, and *A* is large. The characteristic scale *s** also reflects this: in F3 the most variance is lost at 6.6 px, the width of the chlorotic and necrotic patches, whereas in F1 it is lost at 1.3 px, the width of the fine veins; in F0 no interior maximum was found up to 16 px, consistent with its softer focus. A comparison of leaves through the global *A* would therefore compare the position of the analysed region on the blade.

Leaves: four ROIs and the pooling ratio. Table 4 shows the R = 4 configuration at *s* = 2 px. In F0 the four quadrants shared the same axis (116–123°), and the pooled *A* equalled the bound of (4) (0.251 against 0.252). In F1 the quadrant axes spanned the whole half-circle (179°, 16°, 71°, 113°), and the pooled *A* was only 31 % of the bound: two quadrants had *A* = 0.35 and 0.25, but they pointed in different directions. F2 and F3 were intermediate (79 % and 88 %): in F2 three quadrants lay near the horizontal and one (29°) deviated, whereas in F3 all four lay within 20° of the horizontal but differed several-fold in anisotropy. The same pattern appears in the ratio of the global *A* to the energy-weighted mean local coherence (*L**): 0.72 in F0, 0.17 in F1, 0.47 in F2 and 0.43 in F3.

Table 4

Leaves, R = 4 at *s* = 2 px: quadrant anisotropy A_r (95 % bootstrap CI) and axis ψ_r; pooled *A*(Ω), right-hand side of the pooling inequality (4) and their ratio

Leaf	*Q1 A (ψ)*	*Q2 A (ψ)*	*Q3 A (ψ)*	*Q4 A (ψ)*	*A(Ω)*	*Bound (4)*	*Ratio*
F0	0.210 (116°)	0.438 (120°)	0.140 (123°)	0.217 (118°)	0.251	0.252	1.00
F1	0.093 (179°)	0.126 (16°)	0.348 (71°)	0.252 (113°)	0.062	0.198	0.31
F2	0.108 (153°)	0.142 (168°)	0.151 (29°)	0.098 (171°)	0.096	0.122	0.79
F3	0.117 (20°)	0.054 (161°)	0.197 (172°)	0.032 (13°)	0.090	0.102	0.88

Leaves: local coherence. Because the regional *A* depends on venation layout, the local field was examined (Figure 3, Table 5). The mean local coherence was 0.341 in F0 and 0.303 in F1, and fell to 0.195 in F2 and 0.190 in F3. In the coherence maps, F0 and F1 show elongated high-coherence ridges following the veins, whereas in F2 and F3 the ridges are broken into short fragments between chlorotic patches. At the block level (Figure 4), $\overline{\kappa}$ decreased with severity (Kendall $\tau = -0.38$, $P = 3 \times 10^{-9}$), the two symptomless leaves did not differ (F0 vs F1, P = 0.60), and the asymptomatic leaf differed from both symptomatic leaves (F1 vs F2, $P = 5 \times 10^{-6}$; F1 vs F3, $P = 1 \times 10^{-6}$). After the common blur of 1.5 px, the means were 0.342, 0.321, 0.204 and 0.208, the

trend persisted (τ = −0.32, P = 6 × 10^{-7}) and F0 and F1 remained indistinguishable (P = 0.99). The block anisotropy A showed the same ordering with a weaker trend (τ = −0.32).

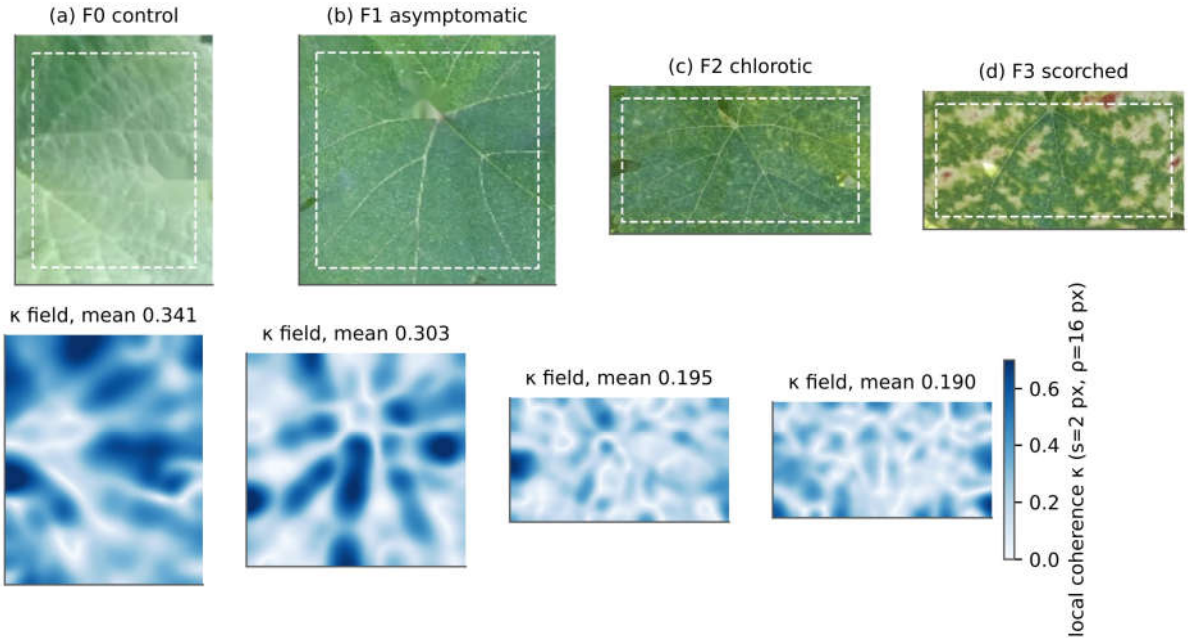


Figure 3. Leaf regions and local coherence. (a–d) Analysed regions F0–F3 (dashed: ROI = 1 after the 24-px margin); inpainted areas in F0 (tendril) and F1 (highlight at the petiolar junction). (e–h) Local coherence $\kappa(\mathbf{x})$ of the L^* channel (s = 2 px, ω = 16 px) with its mean. Leaves from Goufo et al. (2022), CC BY.

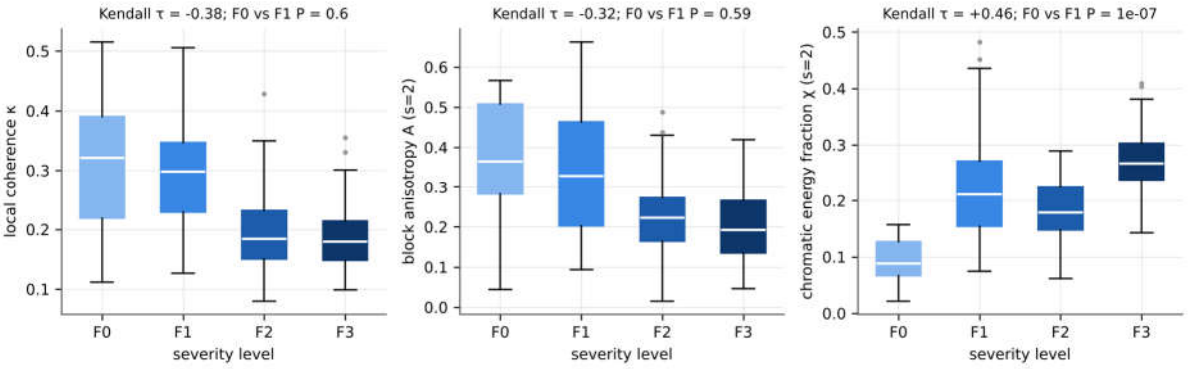


Figure 4. Block-level distributions (48 × 48 px blocks; 24, 36, 45, 36 blocks) of local coherence $\overline{\kappa}$, block anisotropy A and chromatic energy fraction χ at s = 2 px, by severity level, with Kendall's τ over all blocks and the Mann–Whitney P-value for F0 vs F1. Boxes: interquartile range; white line: median.

Table 5

Leaves: local and colour descriptors (s = 2 px). Mean coherence of L^* and of the colour tensor $\mathbf{J}_{Lab}$ (ω = 16 px); block medians [interquartile range]; trend over severity (Kendall τ, 141 blocks) and robustness to a common blur of 1.5 px

Quantity	*F0*	*F1*	*F2*	*F3*	*τ (P)*	*After blur: τ; F0 vs F1 P*
$\overline{\kappa}$ (L^*), whole ROI	0.341	0.303	0.195	0.190	—	—
$\overline{\kappa}$ ($\mathbf{J}_{Lab}$), whole ROI	0.313	0.293	0.201	0.192	—	—
Pooling ratio $A/\overline{\kappa}_E$ (L^*)	0.72	0.17	0.47	0.43	—	—
$\overline{\kappa}$, blocks	0.321 [0.219, 0.390]	0.298 [0.229, 0.347]	0.184 [0.150, 0.232]	0.179 [0.149, 0.214]	−0.38 (3×10^{-9})	−0.32; 0.99
A, blocks	0.365 [0.282, 0.508]	0.328 [0.202, 0.464]	0.223 [0.164, 0.273]	0.192 [0.135, 0.266]	−0.32 (4×10^{-7})	−0.28; 0.61
χ, blocks	0.088 [0.066, 0.127]	0.211 [0.154, 0.271]	0.179 [0.148, 0.224]	0.267 [0.237, 0.303]	+0.45 (7×10^{-13})	+0.36; < 0.001
R_4, blocks	0.011 [0.006, 0.014]	0.007 [0.004, 0.011]	0.005 [0.004, 0.008]	0.005 [0.004, 0.009]	−0.18 (0.004)	−0.18; 0.15

Interpretation. Local coherence measures how strongly oriented the texture is within a window, irrespective of how the orientation varies across the region; it is a ratio of eigenvalues and is therefore unchanged by photographic gain. Its decrease from symptomless to symptomatic leaves is the expected signature of chlorosis and necrosis: the veins remain, but the interveinal tissue acquires patches with edges in all directions, which add gradient energy without a common direction. The absence of a difference between F0 and F1 means that, in these images, the leaf of an infected vine that had not developed foliar symptoms was not distinguished from the control by its texture. The contrast between F1 and F2/F3 is the most reliable in the data set, because these three leaves come from wood-infected vines photographed in the same way.

Leaves: colour and angular harmonics. Table 6 gives the CIELAB means, the chromatic energy fraction and the harmonics of D1. The b^* coordinate (yellowness) increased from 15.2–15.6 in F0–F1 to 22.1 in F2 and 29.1 in F3, in agreement with chlorosis. At s = 1–2 px, colour carried 9–10 % of the gradient energy in F0, 11–23 % in F1 and F2 and 22–28 % in F3; at coarser scales, χ was largest in F1 (0.69 at s = 8 px), where slow green-to-green shading across the blade dominates. At the block level, χ increased with severity (τ = +0.45), but its largest single step was between F0 and F1 ($P < 0.001$), the pair that differs in photograph rather than in symptoms. The colour tensor changed the mean coherence little (0.313 against 0.341 in F0, 0.192 against 0.190 in F3). The second harmonic of D1 followed the regional A ($3R_2$ = 0.20, 0.02, 0.06 and 0.06, against $A(L^*)$ = 0.26, 0.06, 0.10 and 0.09), as expected from (5), with the magnitude-weighted moment smaller than the energy-weighted one. The fourth harmonic was small in all leaves (R_4 = 0.0007–0.0038 at s = 2 px); only F0 exceeded its isotropic floor, and the identity $c_4(\mathrm{D2}) = 0$ held to within 1.2×10^{-16} (Figure 5).

Table 6

Leaves: CIELAB means, chromatic energy fraction χ at four scales, and harmonics of D1 (L^*, s = 2 px, L = 8) with the 95th percentile of 100 isotropic surrogates in brackets

Leaf	*L**	*a**	*b**	*χ (s = 1 / 2 / 4 / 8)*	*R_2 [floor]*	*R_4 [floor]*
F0	70.1	−20.6	15.2	0.102 / 0.088 / 0.130 / 0.233	0.066 [0.016]	0.0038 [0.0021]
F1	58.9	−26.3	15.6	0.108 / 0.227 / 0.470 / 0.685	0.006 [0.006]	0.0008 [0.0012]
F2	52.7	−25.6	22.1	0.106 / 0.189 / 0.350 / 0.548	0.020 [0.005]	0.0007 [0.0011]
F3	57.8	−20.5	29.1	0.216 / 0.280 / 0.335 / 0.375	0.019 [0.009]	0.0010 [0.0018]

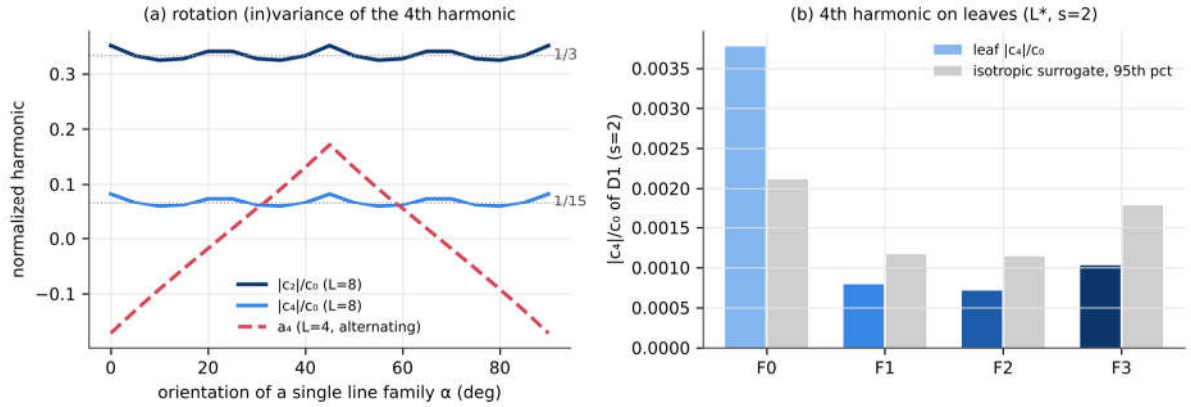


Figure 5. Angular harmonics of D1. (a) Single line family rotated from 0° to 90°: the normalized harmonics R_2 and R_4 obtained with eight orientations stay close to 1/3 and 1/15 (dotted), whereas the alternating component a_4 available with four orientations changes sign with the rotation. (b) R_4 of the leaves (L^*, s = 2 px) against the 95th percentile of isotropic surrogates.

Interpretation. The yellowing of chlorotic and scorched leaves is measured directly by b^*, and the increase of χ at the finest scales in F3 reflects the sharp yellow–green borders of the tiger stripes. The chromatic fraction is, however, not a reliable comparator between photographs: the control leaf is the most brightly exposed and least saturated, and its low χ cannot be separated from that exposure. The fourth harmonic, which in theory detects crossing line networks that the anisotropy index misses, was too weak in these photographs to be useful: the reticulate venation of grapevine leaves is not a network of two dominant families at right angles, and at the resolution available the minor veins contribute little gradient energy. Proposition 3 thus explains why a fourth-order orientation descriptor needs eight orientations, but the data do not support its use for these leaves.

Trunk sections: radial-tangential analysis. Figure 6 and Table 7 summarize the wood. In the control section L0, the six annuli beyond 0.3R had positive radiality (+0.05 to +0.23 at s = 2 px), i.e. ray-dominated texture, while the two innermost annuli, which contain the pith and its boundary, were concentric (−0.63 and −0.15). With increasing severity, positive radiality disappeared from the outer wood: the mean ρ of the three outermost annuli was +0.13, +0.07, −0.07 and −0.21 for L0–L3. The colour front (half-way radius of L^*) moved outward from 0.18R in L0 (the pith) to 0.24R, 0.35R and 0.58R in L1–L3, and in each section the annulus of minimum radiality lay within about one annulus width (0.12R) of it (0.11, 0.13, 0.23 and 0.71R; largest difference 0.13R, in L3). Pooled in image coordinates, the control section had A = 0.062 and in the moving frame A = 0.006 with ρ = −0.005, because the concentric pith boundary and the radial rays cancel within the whole disc; the moving frame becomes informative only per annulus.

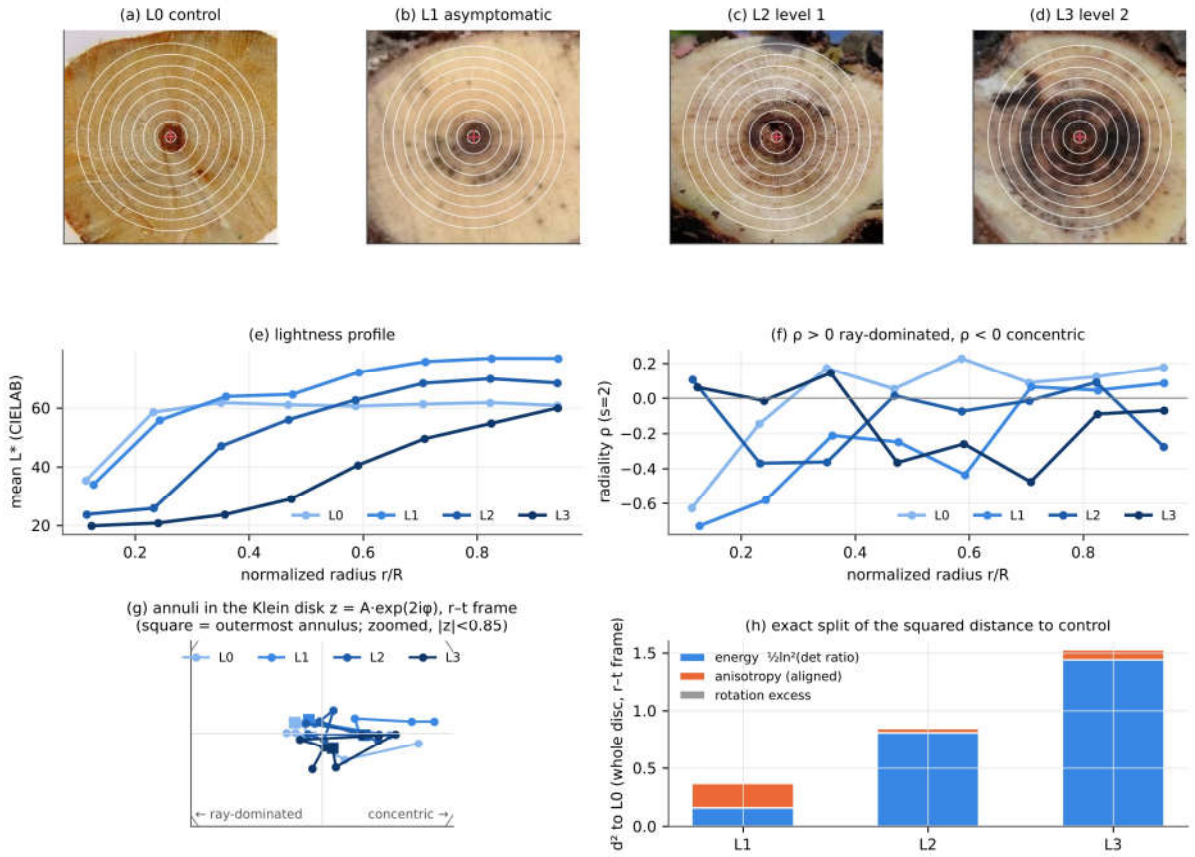


Figure 6. Trunk cross-sections. (a–d) Sections L0–L3 with the pith (+) and the eight annuli. (e) Mean L^* and (f) radiality ρ (s = 2 px) against normalized radius. (g) Annuli in the Klein disk of the radial–tangential frame (right: concentric; left: ray-dominated; square: outermost annulus). (h) Decomposition (8) of the squared distance between the whole-disc matrix of each section and that of the control. Sections from Goufo et al. (2022), CC BY.

Table 7

Trunk sections (s = 2 px unless stated): colour front and radiality minimum (fraction of R), radiality of the outer wood, whole-disc moving-frame quantities, and distance to the control with its decomposition (8), given as the square roots of the three terms, so that d² is the sum of their squares.

Section	*Colour front*	*Min ρ at (value)*	*Outer ρ (3 annuli)*	*Annuli ρ > 0*	*Disc ρ*	*Disc A^{rt}*	*d to L0*	*√Energy / √anisotropy / √rotation*	*d (s = 4)*
L0	0.18	0.11 (−0.63)	+0.13	6/8	−0.005	0.006	—	—	—
L1	0.24	0.13 (−0.73)	+0.07	3/8	−0.315	0.318	0.61	0.40 / 0.46 / 0.05	0.67
L2	0.35	0.23 (−0.37)	−0.07	3/8	−0.140	0.143	0.92	0.90 / 0.20 / 0.04	1.32
L3	0.58	0.71 (−0.48)	−0.21	2/8	−0.197	0.212	1.24	1.20 / 0.30 / 0.02	2.08

Interpretation. In sound wood, the dominant fine-scale structure is the system of rays, which the moving frame reads as positive radiality. Wood necrosis in esca develops around the pith and spreads outward as a discoloured zone with concentric boundaries and dark spots (Mugnai et al., 1999); both add radial gradients and turn the texture concentric, and in the analysed sections the radiality minimum lay close to the colour front. The distance to the control increased across the four analysed sections (0.61, 0.92, 1.24 at s = 2 px; 0.67, 1.32, 2.08 at s = 4 px), but in L2 and L3 it was carried almost entirely by the energy term (95 % and 94 % of d²), the only term of (8) that is not protected against differences between photographs; L0 was photographed on a white

background under different light. Only in L1 did the contrast-invariant anisotropy term dominate (0.46^2 = 57 % of $d^2 = 0.61^2$). The increasing distance is therefore consistent with the severity classes but cannot by itself be attributed to the tissue; the within-section profiles, which share the photograph, are the more reliable reading.

External section: labelled zones and the necrotic front. Table 8 and Figure 7 give the analysis of the section of Kenfaoui et al. (2022). Healthy wood (B) had L^* = 70.5, a texture axis close to horizontal (ψ = 177° at s = 2 px) and A = 0.24. The three affected zones were each separated from B by a different term of (8) at s = 2 px. White rot (A) had similar energy (tr **J** = 0.84 against 0.73) and similar anisotropy (0.25), but its axis was rotated by 89° (ψ = 88°): the rotation term ($\surd$ = 0.71) accounted for about 92 % of d^2 (0.71^2 against 0.74^2). The interaction border (L) had a similar gradient energy (energy term 0.00) but was much more anisotropic (A = 0.60), and the anisotropy term dominated ($\surd$ = 0.64, 69 % of d^2). Sectorial necrosis (S) was smoother (tr **J** = 0.22) and was separated mainly by energy ($\surd$ = 1.71, 86 % of $d^2 = 1.84^2$). At s = 4 and 8 px the terms mixed (for example, L: anisotropy 0.72 and rotation 0.72 at s = 4 px).

Table 8

External section (Kenfaoui et al., 2022, Figure 4b): CIELAB lightness, anisotropy, texture axis, local coherence (ω = 8 px) and trace of **J** at s = 2 px for zones labelled by the authors, and distance to healthy wood (B) with its decomposition (8), given as the square roots of the three terms (d^2 is the sum of their squares)

Zone (authors' label)	*L**	*A*	*ψ*	$\overline{\kappa}$	*tr* **J**	*d to B*	*√Energy*	*√Anisotropy*	*√Rotation*
B, healthy wood	70.5	0.241	177°	0.456	0.73	—	—	—	—
A, white rot	37.7	0.252	88°	0.411	0.84	0.74	0.20	0.02	0.71
L, border (interaction zone)	54.5	0.602	157°	0.545	0.89	0.77	0.00	0.64	0.42
S, sectorial necrosis	61.3	0.231	86°	0.427	0.22	1.84	1.71	0.01	0.68

Along the transect (Figure 7c–e), L^* fell most steeply at a depth of about 276 px and reached its minimum at about 387 px. The texture axis stayed between −18° and +6° in the healthy wood and switched between the windows centred at 380 and 396 px, at both s = 2 and 4 px, remaining at 64–97° throughout the dark band. The rotation term (square root) of the distance to the healthy window was ≤ 0.31 before the switch and ≥ 0.66 after it, at both scales. The energy term, in contrast, fluctuated up to 1.2 within the healthy wood itself, because of the streaks of black spots (P) crossing it, and did not locate the boundary.

Interpretation. The decomposition separates the zones in a way that agrees with their description by plant pathologists: white rot is a reorganization of wood structure (a change of the dominant direction), the border is a narrow zone of strongly oriented, streaky necrosis, and sectorial necrosis is a smoothing of the wood with loss of fine contrast. Along the transect, the steepest change in colour preceded the change in structure by about 110 px, i.e. the outer part of the dark band is discoloured wood that keeps the orientation of healthy wood. This is consistent with the description of the border as an interaction zone between the host and the advancing decay (Kenfaoui et al., 2022), and illustrates the value of a contrast-invariant term: the rotation component, unlike lightness or energy, marked an orientation change along the transect that was not visible as a single edge in this image.

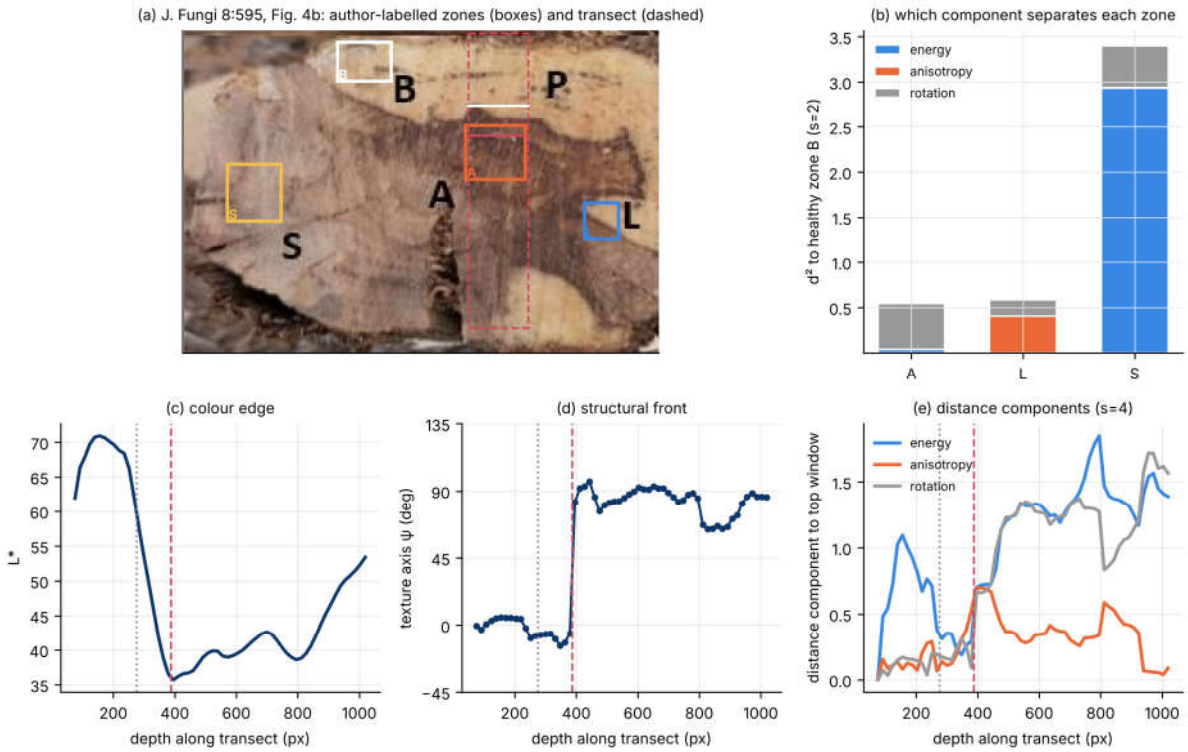


Figure 7. External check on an esca-affected trunk section. (a) Zones placed beside the authors' labels (B, healthy wood; A, white rot; L, interaction border; S, sectorial necrosis; letters not analysed) and the transect (dashed); white line: colour edge; red line: structural front. (b) Decomposition (8) of d^2 to the healthy zone at s = 2 px. (c) L^*, (d) texture axis ψ and (e) distance components to the first window along the transect (s = 4 px); dotted: onset of the colour change; dashed: switch of the texture axis. Image reproduced from Kenfaoui et al. (2022), Figure 4b, under the CC BY 4.0 licence; overlays and panels (b–e) added by the author.

Discussion. The images analysed here support five statements, each within the limits of single published photographs.

First, the regional anisotropy index of a leaf is not a symptom descriptor. In both the single- and the four-ROI configuration, A was governed by the position of the region relative to the main veins: high where the region contained nearly parallel secondary veins (F0), low where it contained the petiolar junction (F1). The pooling inequality (4) explains the mechanism quantitatively (ratio of the pooled A to the bound of (4): 1.00 in F0, 0.31 in F1; ratio to the mean local coherence: 0.72 and 0.17), and the same mechanism would affect any regional orientation descriptor computed on leaves with palmate venation. The practical conclusion is that orientation information on leaves must be read from the local field or after alignment to the venation, not from a regional average.

Second, the mean local coherence showed the clearest association with foliar symptoms in the analysed images. It decreased by about 40 % from the symptomless to the symptomatic leaves, it is invariant to photographic gain by construction, and the decrease survived a common blur that equalized the high-frequency content of the photographs. Because the blocks come from one leaf per class, this association is descriptive and has to be confirmed on independent leaves. Its interpretation is direct: chlorosis and necrosis add interveinal edges without a shared direction, diluting the oriented signal of the venation. The descriptor did not, however, separate the asymptomatic leaf of an infected vine from the control. Foliar symptoms of esca are intermittent and may be absent in vines with extensive wood symptoms (Lecomte et al., 2012), and the metabolite differences between asymptomatic and symptomatic leaves reported for these plants (Goufo et al., 2022) need not have a visible texture counterpart at the resolution of a field photograph.

Third, the Klein-disk decomposition (Proposition 4) turns a single distance into three readings with different physical meanings and different sensitivity to the camera. On the external section, the three affected zones labelled by the authors were each separated from healthy wood by a different term, white rot by rotation, the border by anisotropy and sectorial necrosis by energy, and along the transect the rotation term marked an orientation change that the energy term, disturbed by black-spot streaks in healthy wood, did not. On the trunk sections of different photographs, the same decomposition showed that the increase of the distance across the four sections was carried by the energy term, the only term not protected against differences of acquisition. Reporting the decomposition rather than the total distance is therefore not a refinement but a condition for interpreting comparisons between images taken under different conditions. The result is general: it applies to any pair of 2 × 2 structure matrices, including those of the earlier analyses of muscle histology (Ţălu, 2026, 2027b), and it shows that the familiar pair (A, ψ) are Klein-disk coordinates, which explains why differences in anisotropy near $A = 1$ weigh more than the same differences near isotropy (through artanh A).

Fourth, radial anatomy requires a radial frame. Pooled in image coordinates, the control trunk section was almost isotropic ($A = 0.06$) despite its conspicuous rays; in the moving frame, its outer wood had consistently positive radiality, and the loss of this radiality with severity, together with the outward displacement of the radiality minimum with the colour front, is consistent with the progression of wood necrosis described for esca, expressed in terms of structure rather than colour, although four sections cannot establish it. The frame needs only the position of the pith and involves no resampling of the image.

Fifth, some of the proposed quantities did not prove useful on these data, and this is reported as a result. The fourth angular harmonic, which in theory detects networks of crossing lines that the anisotropy index cannot see, was close to or below its isotropic floor in all leaves, and the chromatic energy fraction, although it increased with severity, could not be separated from the exposure of the control photograph. Proposition 3 remains relevant for the design of the tensor: it shows that a fourth-order orientation descriptor cannot be obtained from four orientations, so that any study intending to use it must sample at least eight.

The approach is complementary to colour segmentation and to learned classifiers used for plant disease detection (Barbedo, 2013; Mahlein, 2016). It does not require lesions to be delimited, its quantities have explicit geometric meaning, and the decomposition makes the dependence on acquisition conditions explicit. Its natural next step is a standardized acquisition, with fixed illumination, a colour reference and a scale bar, of replicated leaves and sections from vines of known status, which would allow the energy term and the chromatic fraction to be compared between images and the descriptors to be tested against visual scores and laboratory diagnosis.

Limitations. Only one published figure with one leaf and one trunk section per class, and one external section, were analysed; there are no biological replicates, and the block-level tests describe the separation of regions within these images, not differences between populations of vines. The photographs differ in exposure, white balance, background and effective resolution (F0 and L1 are notably softer), and no scale bar or colour reference is available, so lengths are in pixels and colour comparisons between photographs are descriptive. The leaf regions were placed by hand to avoid background and overlapping leaves, two small areas were inpainted, and the pith positions and outer radii of the sections were set visually. The zones of the external section were placed beside the authors' letters, which mark points rather than outlines, and the image is soft, so only scales of 2 px and above were used. Leaves are curved and were photographed obliquely, so perspective may alter local orientations. The isotropic surrogates are Gaussian and do not reproduce the non-Gaussian intensity distributions of plant tissue, so exceeding their floor indicates departure from this null model rather than a biological effect; P-values are not corrected for multiple testing. Finally, the results do not establish diagnostic performance, which requires calibrated, replicated data and comparison with baseline descriptors.

Conclusions. A hierarchical descriptor tensor indexed by channel, scale, orientation and region was extended with an exact decomposition of the distance between structure matrices into energy, anisotropy and rotation through the Beltrami–Klein model, with the harmonic content of the orientation profile of the mean absolute derivative, with the colour form of the pooling inequality and with a radial–tangential frame. Applied to published photographs of grapevine leaves and trunk sections affected by esca, it showed that regional leaf anisotropy reflects venation layout rather than symptoms, that mean local coherence was lower in the symptomatic than in the symptomless leaves, that ray-dominated texture is lost from the outer wood with increasing severity, and that the components of the distance separate white rot, the interaction border and sectorial necrosis and mark an orientation change inside the colour edge along the analysed transect. The decomposition also identifies which differences between photographs can be caused by contrast alone. These are exploratory, interpretable and internally consistent readings on the analysed images that motivate the use of the tensor for the quantitative description of esca symptoms in replicated, calibrated studies; diagnostic value is not claimed.

Acknowledgement. The author thanks the authors of Goufo et al. (2022) and Kenfaoui et al. (2022) for publishing their images under an open licence.

Author Contributions. Ştefan Ţălu contributed to all aspects of the work.

Conflicts of Interest. The author declares that there is no conflict of interest.

Copyright and Permissions. Figure 2 and the source panels of Figures 3 and 6 are reproduced from Goufo et al. (2022), and Figure 7a from Kenfaoui et al. (2022), open-access articles published by MDPI under the Creative Commons Attribution (CC BY) licence, which permits reuse with appropriate citation; the source and licence are stated in each caption. Overlays and all other figures were produced by the author. The descriptor tensor and its verification are described in earlier publications (Ţălu, 2027a); no figure, table or result of those publications is reproduced here.

Data Availability. The analysis code, region coordinates and numerical results supporting the findings of this study are available from the corresponding author upon request.

Use of generative AI. During the preparation of this manuscript, the author used GPT-6 Astra to assist in the preparation of one figure. The AI-assisted visual material was subsequently reviewed and edited by the author, who takes full responsibility for the accuracy, originality, and integrity of all content in the manuscript.

Funding. This research received no external funding.

References

Barbedo, J. G. A. (2013). Digital image processing techniques for detecting, quantifying and classifying plant diseases. *SpringerPlus, 2*, 660. https://doi.org/10.1186/2193-1801-2-660

Bertsch, C., Ramírez-Suero, M., Magnin-Robert, M., Larignon, P., Chong, J., Abou-Mansour, E., Spagnolo, A., Clément, C., & Fontaine, F. (2013). Grapevine trunk diseases: Complex and still poorly understood. *Plant Pathology, 62*(2), 243–265. https://doi.org/10.1111/j.1365-3059.2012.02674.x

Bhatia, R. (2007). *Positive definite matrices*. Princeton University Press.

Bigün, J., & Granlund, G. H. (1987). Optimal orientation detection of linear symmetry. In *Proceedings of the IEEE First International Conference on Computer Vision* (pp. 433–438). IEEE Computer Society, London.

CIE (2004). *Colorimetry* (3rd ed., CIE Publication 15:2004). Commission Internationale de l'Éclairage.
Claverie, M., Notaro, M., Fontaine, F., & Wéry, J. (2020). Current knowledge on grapevine trunk diseases with complex etiology: A systemic approach. *Phytopathologia Mediterranea, 59*(1), 29–53. https://doi.org/10.36253/phyto-11150
Depeursinge, A. (2017). Multiscale and multidirectional biomedical texture analysis: Finding the needle in the haystack. In A. Depeursinge, O. S. Al-Kadi, & J. R. Mitchell (Eds.), *Biomedical texture analysis* (pp. 29–53). Academic Press.
Di Zenzo, S. (1986). A note on the gradient of a multi-image. *Computer Vision, Graphics, and Image Processing, 33*(1), 116–125. https://doi.org/10.1016/0734-189X(86)90223-9
Freeman, W. T., & Adelson, E. H. (1991). The design and use of steerable filters. *IEEE Transactions on Pattern Analysis and Machine Intelligence, 13*(9), 891–906. https://doi.org/10.1109/34.93808
Garczyk, Ż., Stach, S., Ţălu, Ş., Sobola, D., & Wróbel, Z. (2017). Stereometric parameters of butterfly wings. *Journal of Biomimetics, Biomaterials and Biomedical Engineering, 31*, 1–10. https://doi.org/10.4028/www.scientific.net/JBBBE.31.1
Ghalati, M. K., Nunes, A., Ferreira, H., Serranho, P., & Bernardes, R. (2022). Texture analysis and its applications in biomedical imaging: A survey. *IEEE Reviews in Biomedical Engineering, 15*, 222–246. https://doi.org/10.1109/RBME.2021.3115703
Goufo, P., Singh, R. K., & Cortez, I. (2022). Metabolites differentiating asymptomatic and symptomatic grapevine plants (*Vitis vinifera* 'Malvasia-Fina') infected with esca complex disease-associated fungi. Biology and Life Sciences Forum, 11(1), 87. https://doi.org/10.3390/IECPS2021-11923
Haralick, R. M., Shanmugam, K., & Dinstein, I. (1973). Textural features for image classification. *IEEE Transactions on Systems, Man, and Cybernetics, SMC-3*(6), 610–621. https://doi.org/10.1109/TSMC.1973.4309314
Kass, M., & Witkin, A. (1987). Analyzing oriented patterns. *Computer Vision, Graphics, and Image Processing, 37*(3), 362–385. https://doi.org/10.1016/0734-189X(87)90043-0
Kendall, M. G. (1938). A new measure of rank correlation. *Biometrika, 30*(1–2), 81–93. https://doi.org/10.1093/biomet/30.1-2.81
Kenfaoui, J., Radouane, N., Mennani, M., Tahiri, A., El Ghadraoui, L., Belabess, Z., Fontaine, F., El Hamss, H., Amiri, S., Lahlali, R., & Ait Barka, E. (2022). A panoramic view on grapevine trunk diseases threats: Case of Eutypa dieback, Botryosphaeria dieback, and esca disease. *Journal of Fungi, 8*(6), 595. https://doi.org/10.3390/jof8060595
Künsch, H. R. (1989). The jackknife and the bootstrap for general stationary observations. *The Annals of Statistics, 17*(3), 1217–1241. https://doi.org/10.1214/aos/1176347265
Lecomte, P., Darrieutort, G., Liminana, J.-M., Comont, G., Muruamendiaraz, A., Legorburu, F.-J., Choueiri, E., Jreijiri, F., El Amil, R., & Fermaud, M. (2012). New insights into esca of grapevine: The development of foliar symptoms and their association with xylem discoloration. *Plant Disease, 96*(7), 924–934. https://doi.org/10.1094/PDIS-09-11-0776-RE
Lindeberg, T. (1998). Feature detection with automatic scale selection. *International Journal of Computer Vision, 30*(2), 79–116. https://doi.org/10.1023/A:1008045108935
Mahlein, A.-K. (2016). Plant disease detection by imaging sensors – Parallels and specific demands for precision agriculture and plant phenotyping. *Plant Disease, 100*(2), 241–251. https://doi.org/10.1094/PDIS-03-15-0340-FE
Mann, H. B., & Whitney, D. R. (1947). On a test of whether one of two random variables is stochastically larger than the other. *The Annals of Mathematical Statistics, 18*(1), 50–60. https://doi.org/10.1214/aoms/1177730491
Mardia, K. V., & Jupp, P. E. (2000). *Directional statistics*. John Wiley & Sons.

Moakher, M. (2005). A differential geometric approach to the geometric mean of symmetric positive-definite matrices. *SIAM Journal on Matrix Analysis and Applications, 26*(3), 735–747. https://doi.org/10.1137/S0895479803436937
Mugnai, L., Graniti, A., & Surico, G. (1999). Esca (black measles) and brown wood-streaking: Two old and elusive diseases of grapevines. *Plant Disease, 83*(5), 404–418. https://doi.org/10.1094/PDIS.1999.83.5.404
Pennec, X., Fillard, P., & Ayache, N. (2006). A Riemannian framework for tensor computing. *International Journal of Computer Vision, 66*(1), 41–66. https://doi.org/10.1007/s11263-005-3222-z
Petrescu-Mag, I. V., Ţălu, Ş., & Şahin, D. (2026). Fractal, multifractal and entropy-based approaches in aquaculture: An integrative review. *Aquaculture, Aquarium, Conservation & Legislation, 19*(2), 882–898.
Ratcliffe, J. G. (2006). *Foundations of hyperbolic manifolds* (2nd ed.). Springer.
Telea, A. (2004). An image inpainting technique based on the fast-marching method. *Journal of Graphics Tools, 9*(1), 23–34. https://doi.org/10.1080/10867651.2004.10487596
Theiler, J., Eubank, S., Longtin, A., Galdrikian, B., & Farmer, J. D. (1992). Testing for nonlinearity in time series: The method of surrogate data. *Physica D, 58*(1–4), 77–94. https://doi.org/10.1016/0167-2789(92)90102-S
Traverso, A., Wee, L., Dekker, A., & Gillies, R. (2018). Repeatability and reproducibility of radiomic features: A systematic review. *International Journal of Radiation Oncology, Biology, Physics, 102*(4), 1143–1158. https://doi.org/10.1016/j.ijrobp.2018.05.053
Ţălu, Ş. (2012). Texture analysis methods for the characterisation of biological and medical images. *Extreme Life, Biospeology & Astrobiology, 4*(1), 8–12.
Ţălu, Ş. (2013). Multifractal geometry in analysis and processing of digital retinal photographs for early diagnosis of human diabetic macular edema. *Current Eye Research, 38*(7), 781–792. https://doi.org/10.3109/02713683.2013.779722
Ţălu, Ş. (2015). *Micro and nanoscale characterization of three-dimensional surfaces: Basics and applications*. Napoca Star Publishing House.
Ţălu, Ş. (2026). Application of the hierarchical texture-descriptor tensor to histological muscle sections of *Poecilia reticulata*. *Poeciliid Research, 16*(1), 62-74. https://doi.org/10.67784/0096
Ţălu, Ş. (2027a). A hierarchical tensor framework for quantitative multiscale and multidirectional biomedical texture characterization. *Human & Veterinary Medicine, 19*(1), 32-53. https://doi.org/10.67784/0095
Ţălu, Ş. (2027b). Coherence, alignment and fibre-profile geometry in a hierarchical texture-descriptor tensor: Application to H&E sections of skeletal muscle in wild boar (*Sus scrofa*) and domestic pigs. *Porcine Research, 17*(1), 1–22. https://doi.org/10.67784/0098.
Ţălu, Ş. (2027c). Descriptor-tensor texture analysis of myostatin-edited rabbit muscle: A two-study replication. *Rabbit Genetics, 17*(1), 10–24. https://doi.org/10.67784/0097
Ţălu, Ş. (2027d). Scale and orientation signatures of soil structure in thin sections: A hierarchical descriptor tensor applied to greenhouse soils under conventional, pollution-free and organic management. *Advances in Environmental Sciences*, *19*(1), 53–70. https://doi.org/10.67784/0099
Ţălu, Ş., & Giovanzana, S. (2011). Fractal and multifractal analysis of human retinal vascular network: A review. *Human & Veterinary Medicine, 3*(3), 205–212.
Ţălu, Ş., Stach, S., Sueiras, V., & Ziebarth, N. M. (2015). Fractal analysis of AFM images of the surface of Bowman's membrane of the human cornea. *Annals of Biomedical Engineering, 43*(4), 906–916. https://doi.org/10.1007/s10439-014-1140-3
Zwanenburg, A., Vallières, M., Abdalah, M. A., Aerts, H. J. W. L., Andrearczyk, V., Apte, A., Ashrafinia, S., Bakas, S., Beukinga, R. J., Boellaard, R., Bogowicz, M., et al. (2020). The Image Biomarker Standardization Initiative: Standardized quantitative radiomics for high-throughput image-based phenotyping. *Radiology, 295*(2), 328–338. https://doi.org/10.1148/radiol.2020191145

Received: 20 September 2026. Accepted: 31 October 2026. Published online: 01 November 2026.
Author:
Ştefan Ţălu, The Directorate of Research, Development and Innovation Management (DMCDI), The Technical University of Cluj-Napoca, Constantin Daicoviciu St., no. 15, Cluj-Napoca 400020, Cluj County, Romania, e-mail: stefan.talu@auto.utcluj.ro ; stefan.talu1@gmail.com ; https://orcid.org/0000-0003-1311-7657
This is an open-access article distributed under the terms of the Creative Commons Attribution License (CC-BY 4.0), which permits unrestricted use, distribution and reproduction in any medium, provided the original author and source are credited.
How to cite this article:
Ţălu, Ş. (2026). Hyperbolic geometry of structure matrices in a hierarchical texture-descriptor tensor: multiscale texture of grapevine leaves and wood affected by esca. *Advances in Agriculture & Botanics, 18*(1), 126–145. https://doi.org/10.67784/0100